

## RESEARCH ARTICLE

10.1002/2016JA023510

## Special Section:

Major Results From the MAVEN Mission to Mars

This article is a companion to *Ledvina et al.* [2017] doi:10.1002/2016JA023521.

## Key Points:

- The role of the electron temperature at altitudes below 500 km is examined via hybrid particle code simulations
- The Martian electron temperature controls the ratio of oxygen ion species lost via the temperature sensitive recombination equations
- The electron temperature profile influences the ambipolar electric field changing the loss rate of oxygen ions from Mars

## Correspondence to:

S. H. Brecht,  
sbrecht@pacbell.net

## Citation:

Brecht, S. H., S. A. Ledvina, and B. M. Jakosky (2017), The role of the electron temperature on ion loss from Mars, *J. Geophys. Res. Space Physics*, 122, doi:10.1002/2016JA023510.

Received 24 SEP 2016

Accepted 13 JUN 2017

Accepted article online 7 JUL 2017

## The role of the electron temperature on ion loss from Mars

Stephen H. Brecht<sup>1</sup> , Stephen A. Ledvina<sup>2</sup>, and Bruce M. Jakosky<sup>3</sup> <sup>1</sup>Bay Area Research Corp, Orinda, California, USA, <sup>2</sup>Space Sciences Laboratory, University of California, Berkeley, California, USA, <sup>3</sup>Laboratory for Atmospheric and Space Physics, University of Colorado Boulder, Boulder, Colorado, USA

**Abstract** This paper reports the results of hybrid simulations of the Mars-solar wind interaction. The focus is on the role of the low altitude (<500 km) electron temperature profile on the ionospheric chemistry, dynamics, and loss rates of oxygen ions. It is found that the loss rates of O<sup>+</sup> and O<sub>2</sub><sup>+</sup> from the Martian ionosphere are changed depending on the electron temperature profile being used. Test simulations show that diamagnetic effects (specifically the ambipolar electric field) are an important part of the solar wind interaction with Mars.

**Plain Language Summary** The research reported in this paper examines the role of the ionospheric electron temperature in the dynamic interaction of the solar wind with the Martian ionosphere. The scientific question being addressed is the amount of ionosphere Mars is losing to the solar wind and what are the key parameters that control that loss. This paper examines the control the ionospheric electron temperature exerts on the ion escape process. The research is performed by three dimensional computer simulation of the solar wind interaction with the Martian atmosphere and ionosphere.

## 1. Introduction

The objective of the Mars Atmosphere and Volatile Evolution (MAVEN) mission is to address the atmospheric dynamics of Mars; specifically the loss of the Martian atmosphere [cf. *Jakosky et al.*, 2015]. A major focus is to understand the key parameters that control that loss. In this paper a parameter that might be a key to understanding the physics driving the ion loss is addressed. This parameter is the ionospheric electron temperature. The ambipolar electric field produced by the gradient of the electron pressure,  $p_e = n_e k_B T_e$ , influences the dynamics. It is found that the electron temperature controls the ratio of the oxygen ion species being lost to space via the ion chemistry sensitivity to  $T_e$  at altitudes ranging from 150 to 250 km. In addition, the changes in chemistry lead to changes in the electron density that manifest themselves via the ambipolar term in the electric field,  $\nabla p_e$ . The change in the chemistry also modifies the effective conductivity of the ionosphere and thereby the electrodynamic that drives ion motion. The research reported in this paper couples the electron temperature data from MAVEN [*Ergun et al.*, 2015; *Fowler et al.*, 2015], with results found by *Ergun et al.* [2016] and HALFSHEL hybrid results. Diamagnetic physics and the ambipolar electric field have been included within the HALFSHEL code for decades. In today's simulations, a highly resolved ionosphere is self-consistently produced by photoionization and assorted chemical reactions including recombination using a prescribed electron temperature profile; see *Brecht and Ledvina* [2012]. The  $\nabla p_e$  contribution to the dynamics of the ionosphere are thought to be realistic (if not entirely accurate) given the dynamic nature of the chemistry and the associated electron density coupled with the temperature profiles.

*Ergun et al.* [2016] have suggested that the selection of the electron temperature profile has a significant effect on the composition of ions lost from Mars and perhaps the loss rate. Their conclusions were based on simulations using both one and two-dimensional versions of the Combined Photochemistry and Ion Tracing (CAPIT) model. Conclusions based on the results are limited because CAPIT covers a small spatial region and makes additional assumptions about the magnetic field. Since the HALFSHEL code already contained the ambipolar term,  $\nabla p_e$ , and a temperature profile, it was decided to examine the suggestions made by *Ergun et al.* [2016] and see if they held up within a global 3-D hybrid kinetic code.

The next section will discuss the science questions that were of interest and the motivation for the simulations. The subsequent section of the paper presents a discussion of the temperature profiles used to determine the role of the electron temperature profile. The following section of this paper presents the pertinent information about the HALFSHEL simulations. The next to last section discusses the results and the last section presents the conclusions drawn from this research.

## 2. Science Questions

The science question addressed in this paper is whether the electron temperature profile is a key parameter. Could the electron temperature profiles and the subsequent ambipolar electric fields be responsible for the ion losses calculated in HALFSHEL and ultimately measured by MAVEN? Another question addressed is, Does the electron temperature profile control the ratio of the  $O^+$  to  $O_2^+$  that is being lost?

While *Brain et al.* [2015] report only heavy ion loss rate, it is important to understand why simulations have differed in reporting differing ratios of  $O^+$  to  $O_2^+$ . Again, *Ergun et al.* [2015, 2016] suggest that it is due to the electron temperature profile. However, the limited spatial extent of their simulations meant that they could not be certain. Mars Express, MEX, data [cf. *Nilsson et al.*, 2011; *Carlsson et al.*, 2006] report loss rates of the two species being close to equal. *Nilsson et al.* [2011] measurements were very limited in energy range (up to 50 eV) because only at these energies could a definitive separation of the oxygen ions be made. Ionospheric composition data from MAVEN published by *Benna et al.* [2015] and *Ergun et al.* [2016] show roughly equal amounts of  $O_2^+$  to  $O^+$  at altitudes up to 500 km. These findings are very interesting because simple photochemical results show the  $O_2^+$  rapidly dropping to near zero above 350 km (cf. *Brecht and Ledvina* [2012] and figures later in this paper).

Many simulations [cf. *Dong et al.*, 2014, and references within] find that the dominant species lost is  $O^+$ . The HALFSHEL simulations typically see  $O_2^+$  as the dominant species. Many simulation models do not have the  $\nabla p_e$  term in them and only use the electron temperature for the chemistry. The results of this research coupled with that of *Ergun et al.* [2016] provide insight into these issues.

To address the questions discussed in this section, a few HALFSHEL simulations were required. One simulation assumes  $\nabla p_e = 0$ ; thus, testing the importance of the  $\nabla p_e$  in general. The subsequent simulations used two different electron temperature profiles. In the first simulation the customary  $T_e$  profile used in *Brecht et al.* [2016] was employed. In the second simulation a profile representing a lower limit of the MAVEN temperature data using the profile fit derived in *Ergun et al.* [2015] was employed. Inserting the lower range of the measured MAVEN temperature into the HALFSHEL code provides an opportunity to study the sensitivity of the simulation results to the  $T_e$  profile.

## 3. Electron Temperature

The electron temperature treatment within the HALFSHEL code is discussed in the following subsections of the paper. As will be discussed below, the temperature profile used in *Brecht et al.* [2016] is a combination of temperature models. Earlier work only used that of *Shinagawa and Cravens* [1989] for lower altitudes and a solution to a temperature equation at higher altitudes. The previous profiles represented the high side of the electron temperature measured by MAVEN. In this work we explore the effect of using a lower limit to  $T_e$  on the solar wind interaction with Mars.

### 3.1. Application of Electron Temperature Equation

The electron temperature profile is held constant below 500 km. Above this altitude equation (1) the electron temperature equation is solved. The altitude for the model transition could be lowered, but the decision was made not to change it. The electron temperature is evolved by solving the following equation

$$\partial T_e / \partial t = -\mathbf{u}_e \cdot \nabla T_e - 3/2 T_e \nabla \cdot \mathbf{u}_e + 2/3 \eta J^2 / n_e \quad (1)$$

where  $\mathbf{u}_e$  is the electron fluid flow velocity and  $\eta$  is the plasma resistivity. Solutions and implementation of equation (1) have been successfully tested and compared to data [cf. *Brecht et al.*, 2016]. The solution to equation (1) provides the changes in  $T_e$  needed to drive the electron impact ionization model in HALFSHEL (cf. *Cravens et al.* [1987] for the cross sections). However, the altitude of interest (below 500 km) means that these processes will not be significant due to the low electron temperatures. For the purposes of this paper there will be no further discussion of this process as each simulation used the same solar wind conditions, thus producing the same ionization of the hot oxygen corona.

### 3.2. Static Electron Temperature Profiles:

*Ergun et al.* [2015, 2016] reported dayside electron temperatures for a variety of MAVEN orbits, specifically the "deep dip" orbits that reached altitudes of  $\sim 130$  km at low solar zenith angles. Large variations in  $T_e$  were

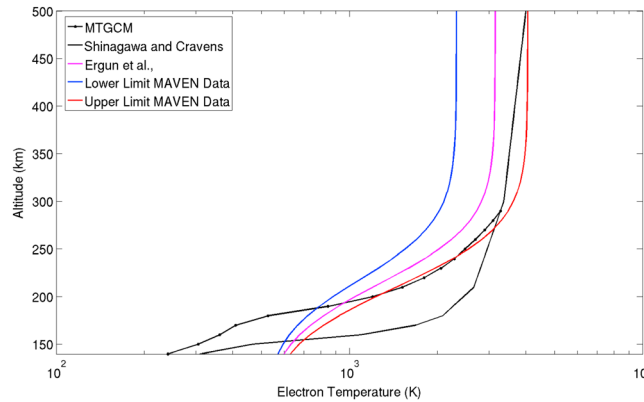


**Figure 1.** Electron temperature profiles used in simulation models. The magenta profile is the best fit electron temperature profile determined from MAVEN data by *Ergun et al.* [2016]. The dotted black curve is the temperature profile from the MTGCM model. The solid black curve is the *Shinagawa and Cravens* [1989] model. The blue line is the temperature profile computed from equation (2) using the lower range of measured electron temperatures. The red line is the fit, equation (2), applied to the high temperature range of the MAVEN data.

measured particularly in the altitude range of 250 km to 500 km. Below 250 km the variations were greatly reduced. *Ergun et al.* [2015] produced an analytic form for the median values of  $T_e$  and then used it in CAPIT *Ergun et al.* [2016]. In the research reported here the analytic form from *Ergun et al.* [2015] was used in HALFSHEL. The form of the fit is reproduced below:

$$T_e(\text{eV}) = (T_{eh}(\text{eV}) + T_{el}(\text{eV}))/2.0 + (T_{eh}(\text{eV}) - T_{el}(\text{eV}))/2.0 \times \tanh((\text{altitude} - z_0)/h_0) \quad (2)$$

where *Ergun et al.* [2015] used  $T_{eh} = 0.271$  eV for the electron temperature at the top of the fit (500 km),  $T_{el} = 0.044$  eV for the electron temperature at the bottom of the fit (~0 km), with the parameters  $z_0 = 241.0$  km and  $h_0 = 60.0$  km coming from the least squares fit of the MAVEN temperature data. The low-altitude temperature for the fit is the same for all profiles.

In earlier simulations the electron temperature profile from *Shinagawa and Cravens* [1989], referred to in this paper as S&C, was used. This profile was developed from Viking measurements that occurred during solar minimum. Simulations reported in *Brecht and Ledvina* [2014] and earlier used S&C. *Brecht et al.* [2016] used a combination of S&C and the electron temperature from the Mars Thermospheric Global Circulation Model, MTGCM. The electron temperatures from the MTGCM model were used for altitudes up to 250 km (the top of the MTGCM grid) and then the S&C profile is used. The MTGCM temperatures were determined from a standard formulation based upon Viking measurements [e.g., *Fox*, 1993]. Recall that the electrons are treated as a fluid and much of the physics to accurately calculate the electron temperature at lower altitudes is not in the code: hence the decision to hold the electron temperature constant consistent with the MTGCM code and S&C. To examine the effect of the extreme (coldest electron temperatures) on the chemistry and the subsequent plasma dynamics,  $T_{eh}$  was chosen to be 0.2 eV at 500 km consistent with cold limit of the data at that altitude. Henceforth, this profile will be called the low  $T_e$  MAVEN fit.

Figure 1 shows the S&C electron temperature profile (black) used in previous simulations and that used from the MTGCM model (dotted black line). In the current simulations the MTGCM electron temperature is smoothly merged into the S&C temperature model at high altitudes. The magenta line is the standard  $T_e$  fit used by *Ergun et al.* [2016] in the CAPIT code. The blue line is the *Ergun et al.* fit applied to the lower range of MAVEN  $T_e$  data as reported by *Ergun et al.* [2015, 2016] and used in the simulation. The red line represents the fit, equation (2), applied at the high-temperature end of the data at 500 km altitude. The high-temperature fit (red line) shows that the S&C profile is representative of the high end of the MAVEN temperature data until slightly above 250 km altitude. Lower than that, S&C is a warmer profile until one reaches about 150 km altitude. The combination of the MTGCM and S&C, MTGCM/S&C, profiles used in many of the simulations is cooler at low altitudes. Recall that the minimum temperature for the fit that produced equation (2) is 510°K (0.04 eV). This minimum is due to instrument limitations.

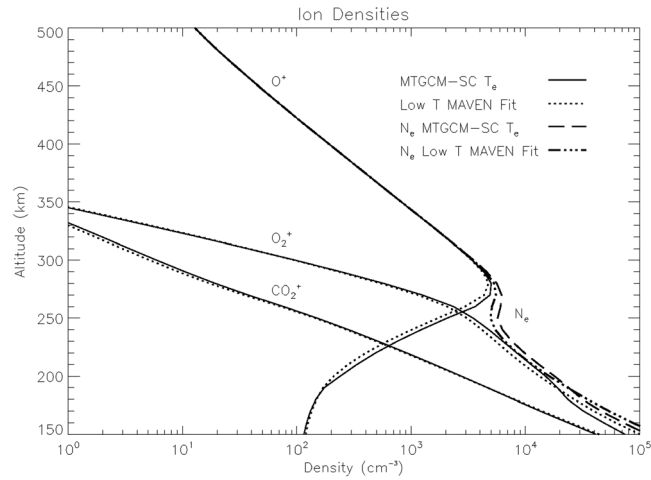


**Figure 2.** The composition of the Martian ionosphere as created by HALFSHEL photochemistry. The profile was created at the subsolar point of the atmosphere using both  $T_e$  fits. The electron density is a sum of the ion densities.

In earlier simulations where only the S&C fit was used, it was assumed that the electron temperature dropped on the nightside of Mars. This assumption was implemented using the solar zenith angle dependence reported by *Singhal and Whitten* [1988]. This approach seemed to be a reasonable since on the Earth's night side the  $T_e$  is measured to be cooler than on the dayside [cf. *Otsuka et al.*, 1998]. In the more recent simulations, it was assumed that the profile was a constant around the planet consistent with the assumption made in the MTGCM code. It would seem that this assumption is not as bad as one would think. *Fowler et al.* [2015] reported  $T_e$  profiles that were surpris-

ingly warm on the nightside. Not only did the temperature profiles not drop off in the nightside of Mars the data suggests that it might be credible to increase the temperature profiles on the nightside.

### 3.3. Effect of the Electron Profiles

The electron temperature is used in calculating the  $\nabla p_e$  term and in the chemistry package [cf. *Brecht and Ledvina*, 2012]. The chemical reactions dependent on  $T_e$  are

$$\text{CO}_2^+ + e \rightarrow \text{CO} + \text{O} \quad 3.5 \times 10^{-7} (300/T_e)^{0.5} \text{cm}^{-3} \text{s}^{-1} \quad (3)$$

$$\begin{aligned} \text{O}_2^+ + e \rightarrow \text{O} + \text{O} \quad & 1.95 \times 10^{-7} (300/T_e)^{0.7} \text{cm}^{-3} \text{s}^{-1} (T_e < 1200 \text{ K}) \\ & 7.38 \times 10^{-8} (1200/T_e)^{0.56} \text{cm}^{-3} \text{s}^{-1} (T_e > 1200 \text{ K}) \end{aligned} \quad (4)$$

Equations (3) and (4) reveal that recombination is reduced if the temperatures are increased. Figure 1 shows that MTGCM/S&C profile used in the past was hotter than the low  $T_e$  MAVEN profile (blue line) and *Ergun et al.* [2015] fit to the MAVEN data (magenta line) down to  $\sim 180$  km altitude. The MTGCM/S&C profile is cooler up to approximately 180 km altitude, thus increasing the recombination rate of the  $\text{CO}_2^+$  and the  $\text{O}_2^+$ . This implies that the "nominal" profiles increase the presence of  $\text{CO}_2^+$  and the  $\text{O}_2^+$  relative to *Ergun et al.* type of profiles above 180 km. Below 180 km altitude the  $\text{O}_2^+$  density increases with the low  $T_e$  MAVEN profile. *Ergun et al.* [2016] discusses the changing recombination rates relative to the chemistry used in the CAPIT code and reaches similar conclusions.

Indirectly, the electron temperature also affects the following equation because we assume that the ion temperature at low altitudes ( $< 500$  km) is equal to the electron temperature.

$$\begin{aligned} \text{O}^+ + \text{CO}_2 \rightarrow \text{O}_2^+ + \text{CO} \quad & 1.1 \times 10^{-9} \text{cm}^{-3} \text{s}^{-1} (T_i < 800 \text{ K}) \\ & 1.1 \times 10^{-9} (800/T_i)^{0.39} \text{cm}^{-3} \text{s}^{-1} (T_i > 800 \text{ K}) \end{aligned} \quad (5)$$

We could calculate the ion temperature from the particle ions, but it is a very time consuming process and the code does not have all of the processes for heat transport as will be discussed later in the paper. The ion temperature-driven reaction does not become temperature dependent until one reaches roughly 180 km for the MTGCM/S&C and the low  $T_e$  MAVEN fit from equation (2). Above 180 km the reaction rate is decreased more by the MTGCM/S&C profiles than by the low-temperature MAVEN fit.

Figure 2 displays the oxygen ion and  $\text{CO}_2^+$  profiles calculated at the subsolar point using the nominal (MTGCM/S&C)  $T_e$  profile and the low  $T_e$  fit from equation (2). One notices that unlike the data reported by

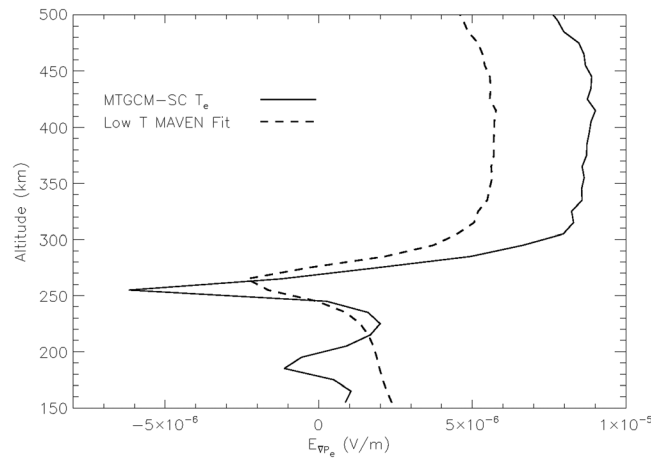


**Figure 3.** The radial ambipolar electric field created when using the two different fits to the electron temperature, Figure 1, and the associated electron densities, Figure 2.

significant sensitivity to the  $T_e$  profile between 180 km and 280 km altitudes. The  $O_2^+$  profile starts to change below 260–270 km and actually switches the ratio between the nominal and low  $T_e$  MAVEN fit at approximately 190 km altitude. None of the ion density profiles undergo large changes due to the change in the electron temperature profile. All of the ion density profile changes are consistent with the changes in the temperature profiles.

The electron density does show significant changes in both magnitude and profile shape below 280 km altitude. The new  $T_e$  profiles will modify the diamagnetic behavior of the plasma and the ambipolar electric field via the  $\nabla p_e$  term. Since  $p_e = n_e k_B T_e$ , the changes in the temperature profile changes the gradient of  $T_e$ . Changes in  $T_e$  also change the chemistry thus changing the gradient of the electron density. These changes will modify the electric fields generated within the ionosphere and subsequent plasma dynamics.

Figure 3 illustrates the changes in the radial electric field,  $E_r$ , as a function of altitude. This plot was made from the subsolar profiles shown in Figure 2. The radial electric field oscillates about zero at the low altitudes (<250 km) and then swings positive for both  $T_e$  profiles above 250 km altitude. Below 250 km the field strength is below  $\pm 5 \mu\text{V/m}$ . Above 250 km altitude the MTGCM/S&C  $T_e$  profile swings up to about  $9 \mu\text{V/m}$  while the low  $T_e$  MAVEN profile reaches about  $5 \mu\text{V/m}$ . In the dynamic situation where plasma advection takes place these values change. However, this figure does illustrate and explain some of the results to be reported in the results section of this paper.

## 4. Model Information

### 4.1. Simulation Parameters

The HALFSHEL hybrid particle code has been described in detail in a variety of papers. The most recent is *Brecht et al.* [2016]. Unlike a fluid code, a particle code uses an Euler-Lagrangian approach. Therefore, a particle code can include multiple overlaid grids for differing purposes because the particle location and velocities are independent of a grid.

The HALFSHEL code uses multiple grids: a Cartesian grid for electromagnetic solves and plasma dynamics and a set of spherical grids for high resolution chemistry and collisions. The spatial resolution in the Cartesian grid is 100 km. The spherical grid where chemistry and collisions are calculated employs 10 km radial resolution (extending from 140 km to 850 km in altitude) and  $1.4^\circ$  in angular resolution. The time resolution is 0.02 s for the plasma advection and the magnetic field evolution and 0.05 s for the chemistry equation solutions. The small time step for the chemistry solver allows accurate solution of the chemistry equations for all situations: solar minimum to solar maximum. It also allows accurate solutions over the range of neutral density variations found in the Mars Thermosphere Global Circulation Model, MTGCM, code. The MTGCM model will be discussed in section 4.2.5. *Brecht et al.* [2016] discuss convergence tests performed

*Benna et al.* [2015] and *Ergun et al.* [2016], the  $O_2^+$  profiles do not reach 500 km. These are equilibrium profiles that are calculated by the HALFSHEL chemistry (integrated for 20,000 s) before plasma advection takes place. As will be discussed later, advection plays a major role in the actual ion densities present in the Martian ionosphere.

The next feature to notice is that  $CO_2^+$  is slightly modified with the changing temperature profile and that the modification occurs at low densities and above 250 km altitude. The oxygen ion profiles do the opposite. They change near and below 250 km altitude. The  $O^+$  profile shows

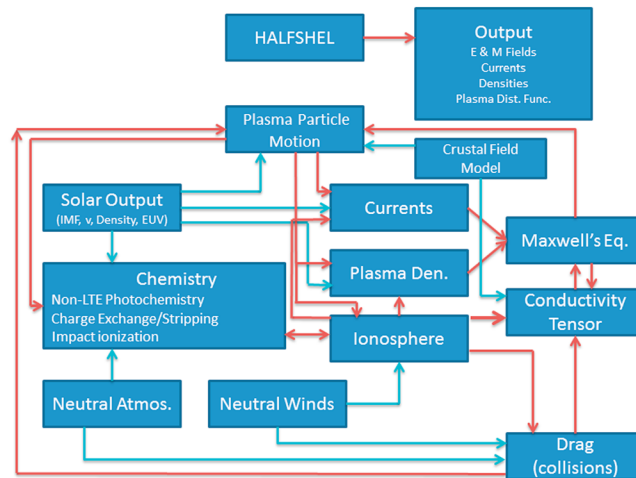


**Figure 4.** Flow chart of the HALFSHEL hybrid code. The cyan lines indicate inputs from models not modified by the functions of the code. The red lines indicate active feedback between models in the code.

with the Cartesian grid. It was found that the ion escape rates were not changed with 150 km or 100 km Cartesian cells. However, in those tests the fine spherical grid was the same for both cases and for the simulations reported in this paper. One final note, at the surface of Mars,  $1^\circ$  represents  $\sim 59$  km. The angular resolution used here ( $1.4^\circ$ ) represents  $\sim 83$  km. Only the radial resolution (10 km) needed to resolve the scale height of the Martian neutral atmosphere is significantly smaller than the 100 km resolution of the Cartesian grid.

The solar wind parameters used in the simulations are as follows: The solar wind speed was 485 km/s, the interplanetary magnetic field, IMF, magnitude was 3 nT with a Parker spiral angle of  $56^\circ$ , and the solar wind density was  $2.7 \text{ H}^+ \text{ cm}^{-3}$ . The rotational axis of the planet is tipped at  $25.19^\circ$  with the orientation determined by the solar longitude, Ls. The solar EUV level used represents a median value of the solar activity at the time of the MAVEN arrival. As represented by the  $F_{10.7}$  proxy at Earth, the EUV level was  $F_{10.7} = 130$ . The photo ionization rates within the chemistry are set to an EUV level represented by the  $F_{10.7}$  proxy adjusted from Earth to Mars using  $1/R^2$  scaling to the appropriate location of Mars. The planet was placed at  $L_s = 270^\circ$ . The neutral atmosphere applied in the set of simulations to be discussed was created for  $L_s = 270^\circ$  and the neutral winds were included in the simulations. The Coordinated Mars Time, MTC, was chosen to orient the geographical longitude of  $270^\circ$  toward the Sun.

#### 4.2. Models Operating With HALFSHEL

Accurate simulation of the solar wind interaction with the Martian ionosphere requires a suite of models for important processes. In the next subsections, these models are briefly discussed. Figure 4 shows a schematic of the HALFSHEL code illustrating the models used and how they are connected to one another.

##### 4.2.1. The Photochemistry Model

The photochemical driven chemistry model produces and maintains the ionosphere in the simulations. However, it is not assumed that the ionosphere is in photochemical equilibrium. The ion-neutral chemical reactions (photochemistry) used in HALFSHEL can be found in *Brecht and Ledvina [2012]*. The reaction set is similar to those reported by *Liu et al. [2001]* and *Ma et al. [2002, 2004]*. Each numerical particle has a density associated with it, and the density is modified by the ion-neutral chemistry using the combined ion densities from particles within a spherical grid cell. New particles are created if the ion production rate exceeds the loss rates within each spherical cell. Otherwise, existing particles have their density decreased by chemical processes.

##### 4.2.2. The Ion Collisional Model

The collisional model addresses particle-by-particle collisions using the high-resolution grid and the velocity of each particle. The HALFSHEL code treats the ion drag by colliding the  $\text{H}^+$ ,  $\text{O}^+$ , and  $\text{O}_2^+$  particles with atmospheric  $\text{CO}_2$  and O using their respective collision cross sections. Currently, heating of the particles, (randomization of their trajectories) is not included. The interaction is simply an energy loss (drag) from the moving particles. This is a “conservative” approach for examining ion loss because it overestimates the energy deposited in the neutrals and underestimates the ion energy. The neutral profiles are untouched; thus, the energy transfer to the neutrals is not accounted for in the simulations, although the ions energy and momentum is changed via neutral winds. The ion-neutral collision frequencies were taken from the expressions in *Shunk and Nagy [2000]* using the neutral polarizability [*Shunk and Nagy, 2000, Table 4.1*]. The ion-ion collisions are not included in the simulations because the ion densities are low with respect to the neutral density.

#### 4.2.3. The Conductivity Model

Hall and Pedersen conductivities are included in the electric field solutions. The generalized electric field including the Hall and Pedersen terms comes from a text by *Mitchner and Kruger* [1973] and replaces the normal simplified electric field equation with a more complex form to encompass the conductivity tensor. The generalized electric field [*Mitchner and Kruger*, 1973] is

$$E = (J + \beta_e \mathbf{J} \times \mathbf{B} + s(\mathbf{B} + \mathbf{B}_0) \times (\mathbf{J} \times (\mathbf{B} + \mathbf{B}_0))) / \sigma - \nabla p_e / (en_e) \quad (6)$$

where the  $\sigma$  is the electron conductivity defined as  $(n_e e^2) / (m_e \nu_{eH})$ ,  $\nu_{eH}$  are the electron collision frequencies (electron-neutral and electron-ion),  $\mathbf{J}$  is the current density,  $\beta_e$  is the electron Hall parameter, and  $(\omega_{en} / \nu_{eH})$  with  $\omega_{en} = eB / cm_e$  is the electron cyclotron frequency.  $\mathbf{B}$  is the evolving magnetic field and  $\mathbf{B}_0$  is the crustal magnetic fields. The "ion slip factor,"  $s$ , is  $((\rho_n / \rho)^2 \beta_e \beta_i)$  where  $\rho_n$  is the neutral mass density,  $\rho$  is the total mass density (ion + neutral), and  $\beta_i$  is the ion Hall parameter  $(\omega_{in} / \nu_{in})$ . The electron-ion collision frequencies are calculated from *Spitzer* [1962]. The electron-oxygen (neutral) and electron-CO<sub>2</sub> (neutral) collision frequencies were taken from *Strangeway* [1996].

The plasma resistivity for the electron Hall and Pedersen terms are computed from the local spherical grid quantities of electron density, ion density, neutral density, and magnetic field at each time step. The ion contribution comes from the ion-neutral collision frequency and the ion cyclotron frequency calculated locally at each spherical grid point, and the electron-ion collision frequency. Note, the  $\nabla p_e$  term in equation (6) produces ambipolar electric fields that can be both parallel and perpendicular to the magnetic field. In *Brecht and Ledvina* [2010] it was found that the HALFSHEL simulations produced parallel electric fields in the tail region of Mars with potential drops consistent with Mars Global Surveyor, MGS, and MEX data. Both the MGS data and the MEX data have revealed the presence of aurora [*Brain et al.*, 2006; *Halekas et al.*, 2008; *Bertaux et al.*, 2005; *Lundin et al.*, 2006a, 2006b; *Leblanc et al.*, 2006, 2008].

#### 4.2.4. The Crustal Magnetic Field Model

The discovery that Mars possessed crustal magnetic fields, see *Acuña et al.* [1998, 1999], required that the HALFSHEL code have a crustal magnetic field model. The crustal magnetic field model from *Purucker et al.* [2000] is embedded in the code. This model returns magnetic field components for altitudes ranging from near surface to beyond  $2 R_m$ . The Martian geographical location, the surface longitude and latitude specifies the crustal magnetic field orientation. The subsolar point of the crustal field models is specified by the solar longitude,  $L_s$ , and Coordinated Mars Time, MTC, where MTC = 0 is longitude 0° at the Airy crater. The code carries the full 3-D crustal field at the resolution of the code. The code includes planetary rotation and inclination; thus, the crustal magnetic fields corotate with the neutral atmosphere.

#### 4.2.5. The Neutral Model

Past research has determined that the chemistry and its response to advection is a crucial part of understanding the ionospheric dynamics and the subsequent loss rates from Mars [*Brecht and Ledvina*, 2012]. The HALFSHEL code has the ability to make use of the full three-dimensional neutral dynamics and couple it to the ionosphere dynamics. In the research reported here a full three-dimensional neutral atmosphere has been placed within the hybrid code, HALFSHEL. However, the coupling is only one way at this point with the neutral density and flows not being affected by the ionospheric dynamics. The neutral atmosphere incorporated with HALFSHEL comes from the Mars Thermospheric Global Circulation Model, MTGCM, code. The MTGCM is a finite difference primitive equation model that self-consistently solves for time-dependent neutral temperatures, neutral-ion densities, and three-component neutral winds over the Mars globe [e.g., *Bougher et al.*, 1999a, 1999b, 2000, 2002, 2004, 2006, 2008; *Bell et al.*, 2007]. The density profiles have been extrapolated above the nominal altitude (250 km) used as an upper boundary for the MTGCM code.

#### 4.2.6. Corotation of the Neutrals

The MTGCM neutral models assume that the atmosphere corotates with the planet. The simulations reported here do not make that assumption. Therefore, the corotation is added to the neutral flows provided from the MTGCM code. The equatorial corotational velocity of Mars ranges from roughly 245 m/s at the surface to slightly more than 280 m/s at 500 km. The MTGCM code indicates that vertical winds can reach 30 m/s while the zonal winds reach velocities (400 m/s) which are in excess of the corotational velocities. The ions created by photochemical processes are given the neutral velocity values at their location as provided by the MTGCM neutral atmosphere plus the correction for corotation velocity. The presence of the corotation velocity will reduce drag on particles being accelerated toward the east (dawn) but increase it for those going westward (dusk). With the presence of the neutral flow fields, the imposed electromagnetic fields from the solar wind,

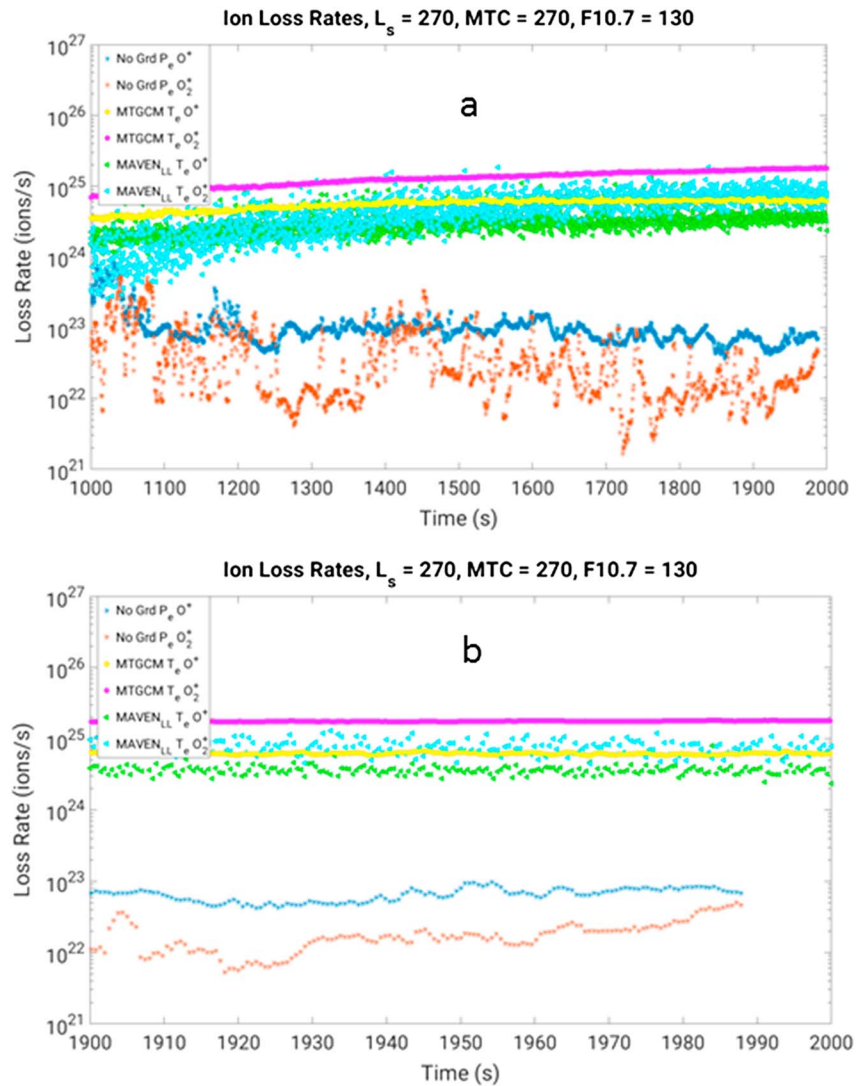


**Figure 5.** (a) Total loss rates (#/s) for  $O^+$  and  $O_2^+$  for the three simulations: blue and red ( $\nabla p_e = 0$ ), purple and gold (nominal case), and cyan and green (low  $T_e$  MAVEN temperature fit). (b) The last 100 s of the data displaying the steady state trend of the loss rate.

and the rotating crustal fields, it is unlikely that the ionosphere is locked into corotation. Whether it is or not is determined self-consistently by HALFSHEL.

### 5. Numerical Results

The HALFSHEL code was run for three cases. The first used the nominal  $T_e$  profile, MTGCM/S&C. The second test was to use the low-temperature MAVEN profile (magenta line) shown in Figure 1. The last test was to turn the ambipolar electric field off,  $\nabla p_e = 0$ .

The loss rates for each simulation are calculated from particles as they pass through a virtual box  $2 R_M$  from the center of the planet. The loss rate results are summarized in Figure 5. The loss rates are plotted as a function of simulation time (seconds) for each oxygen ion species. The simulations are stopped when the loss rates reach a steady state. The exception to this is in the case where  $\nabla p_e$  was turned off (set to 0). The trend for the purposes of this paper was clear and required no further running time.

The blue and red/rust color display the time-dependent loss rate during the course of the simulation for the  $\nabla p_e = 0$  case. The loss rates are noisy and roughly 2 orders of magnitude below the results of the other

**Table 1.** Loss Rates for Each  $T_e$  profile

Electron Profile	$O^+$ Loss Rate (#/s)	$O_2^+$ Loss Rate (#/s)	Total Loss Rate (#/s)
MTGCM and S&C $T_e$	$6.0 \times 10^{24}$	$1.8 \times 10^{25}$	$2.4 \times 10^{25}$
MAVEN low $T_e$	$3.7 \times 10^{24}$	$8.0 \times 10^{24}$	$1.2 \times 10^{25}$

simulations. The  $O^+$  loss is larger than the  $O_2^+$  loss rate. The standard deviation for the last 100 s are  $1.4 \times 10^{22} O^+/s$  and  $9.5 \times 10^{21} O_2^+/s$ .

The nominal simulation (MTGCM/S&C) represented by the gold (almost red when overlaid by the other data, see Figure 5b) and purple symbols is the result reported for the  $MTC = 270^\circ$  and  $F_{10.7} = 130$  case in Brecht *et al.* [2016] with the  $O^+$  loss rate a factor of three smaller than the  $O_2^+$  loss rate. This result is typical of all of the results reported by Brecht and Ledvina to date. The standard deviation for these data are  $2.2 \times 10^{23} O^+/s$  and  $2.5 \times 10^{23} O_2^+/s$ . These results show very little noise.

The simulation results using the fit to the low temperature portion of the MAVEN data are represented by the cyan ( $O_2^+$ ) and green ( $O^+$ ) data. In this case, the  $O^+$  and  $O_2^+$  loss rates show significant noise. The standard deviations for these data are  $6.6 \times 10^{23} O^+/s$  and  $1.8 \times 10^{24} O_2^+/s$ . While the  $O_2^+$  loss rates are higher than

the  $O^+$ , the rates are closer than in the nominal situation. The loss rates shown in Table 1 are obtained by taking the mean of the data for the last 100 s of the series.

If one uses two standard deviations to represent the extent of 90% of the results, one sees that there is an overlap in the oxygen ion loss rates:  $5.0 \times 10^{24} O^+/s$  (upper bound) and  $4.4 \times 10^{24} O_2^+/s$  (lower bound).

To examine the role of plasma advection on the ionospheric ions, cuts through the  $O_2^+$  and  $O^+$  densities on the spherical grid are produced. The cuts are made at  $270^\circ$  longitude and reflect the densities from pole to pole through the subsolar point located at latitude  $-25.19^\circ$  south of the planetary equator. Please note that geographic coordinates are often very different from the Mars Solar Electric, MSE, coordinates or in this case the solar zenith angle coordinates. The MSE is defined by the direction toward the Sun, the magnetic field component perpendicular to the solar wind, and the convection electric field ( $\mathbf{E} = -\mathbf{V} \times \mathbf{B}$ ). In these simulations the MSE north pole is at a geographic latitude of roughly  $65^\circ$ . Figure 6 shows the densities for  $O_2^+$  and  $O^+$  using the MTGCM/S&C  $T_e$  profile (nominal). Figure 6a displays the  $O_2^+$  density for a cut through the subsolar longitude of  $270^\circ$ . Figure 6b

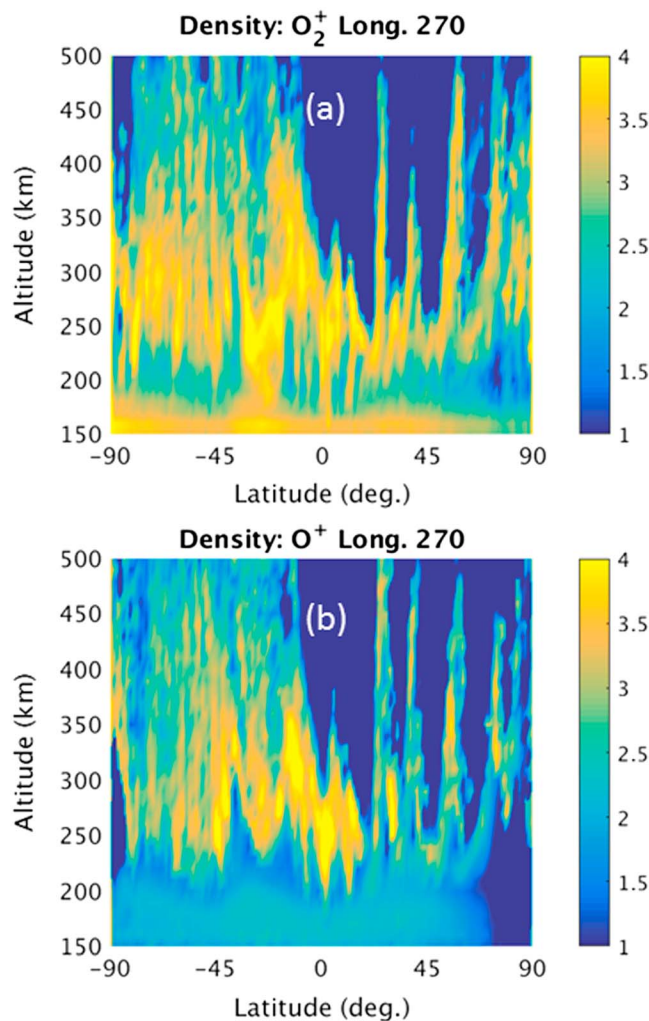


**Figure 6.** Plot along the subsolar longitude versus altitude of (a)  $O_2^+$  density ( $\#/cm^3$ ) and (b)  $O^+$  density ( $\#/cm^3$ ) for nominal  $T_e$  profile. Color bar is in  $\log_{10}$  of density.

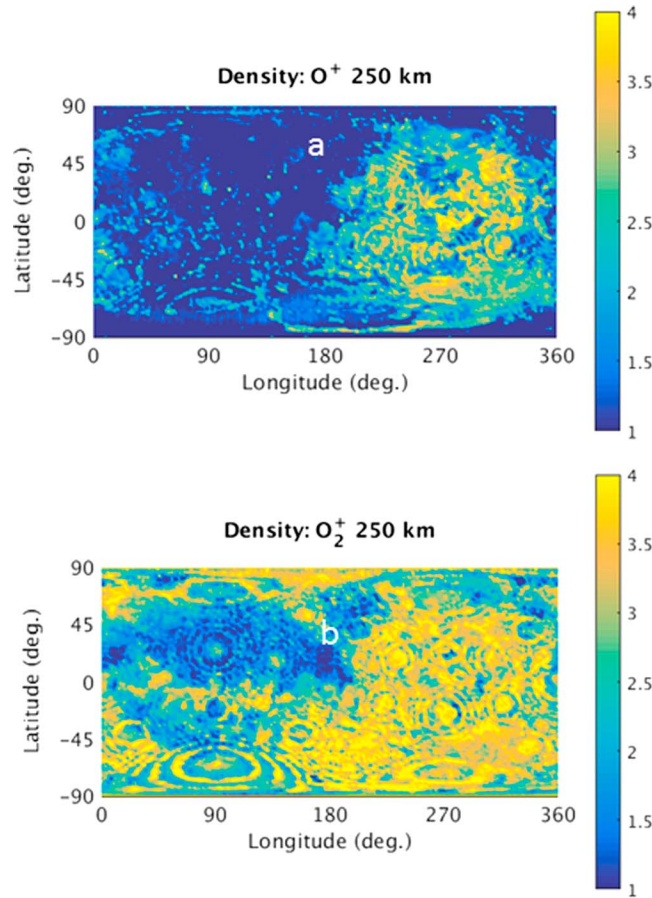


**Figure 7.** (a)  $O^+$  and (b)  $O_2^+$  density ( $\#/cm^3$ ) contours at an altitude of 250 km shown in  $\log_{10}$  levels. The contours are the result of using the MAVEN profile.

two simulations. Examination of Figure 2 reveals that one would expect very similar densities for  $O^+$  and the  $O_2^+$  at 250 km altitude. These figures offer little indication of why the oxygen ion loss rate is twice as high for the nominal case. One might expect unusual dynamics in the subsolar region because the largest crustal magnetic field is nearby, see *Acuña et al.* [1998, 1999], and there seems to be some evidence of the crustal fields exerting their influence in the patterns seen in the figures.

Figures 8a and 8b offer some evidence that the structure might be caused by the crustal magnetic fields. Shown in Figures 8a and 8b are the densities for the  $O^+$  and  $O_2^+$  from the MTGCM/S&C electron temperature profile plotted at a constant altitude, 180 km. At this altitude there is very little plasma motion and the little motion comes from the neutral winds. What structure there is does coincide with the crustal magnetic fields. The day/night terminator is clearly seen in Figures 8a and 8b. Recall that the plots are in geographic coordinates and the crustal magnetic fields do play a nonintuitive role in the advection of the plasma in the tipped rotating planet situation. An example of the nonintuitive behavior of the crustal magnetic fields can be found in plots made of the crustal field location as plotted in MSE coordinates with changing MTC [*Ledvina et al.*, 2017]. Again, the results from the simulation using the low  $T_e$  MAVEN profile produce virtually identical results at 180 km as one would expect based on the results shown in Figure 2.

Another change in the simulation results was noted. This change was in the spectra of the oxygen ions lost to space. In Figure 9 the flux distribution function for both oxygen ion species is plotted as a function of the particle kinetic energy. The units of the distribution are ions/( $cm^2$  s sr eV). The data for this plot was collected via a virtual box at  $2 R_m$  from the center of the planet. All ions passing through this virtual box are collected in a data table which has velocity, location, density, and time of passage. From these data the distribution function can be computed. The solid lines show the  $O^+$  distribution for both  $T_e$  profile simulations, while the

displays the  $O^+$  for the same cut. Both Figures 6a and 6b show structured transport to high altitudes with densities consistent with those reported by *Benna et al.* [2015] and *Ergun et al.* [2016]. Comparison with Figure 2 offers some insight into the role advection plays in the dynamics of the measured ionosphere of Mars. The plots using the low  $T_e$  MAVEN profile show very similar results and thus are not shown.

Figures 7a and 7b display the  $O^+$  and the  $O_2^+$  densities at an altitude of 250 km. These results are from the low  $T_e$  MAVEN simulation. One can clearly see the subsolar region at longitude 270° latitude  $-25.19^\circ$ . The tip of the planet at  $L_s = 270^\circ$  is evident from the photoproduction taking place at the illuminated south pole. This figure also displays the ion density structures found around the planet. One also sees nightside  $O_2^+$  but little nightside  $O^+$ . The nightside  $O_2^+$  is due to advection of the plasma from the dayside. The results from the simulation with the nominal electron temperature profile are not shown because there is little difference between the densities from the

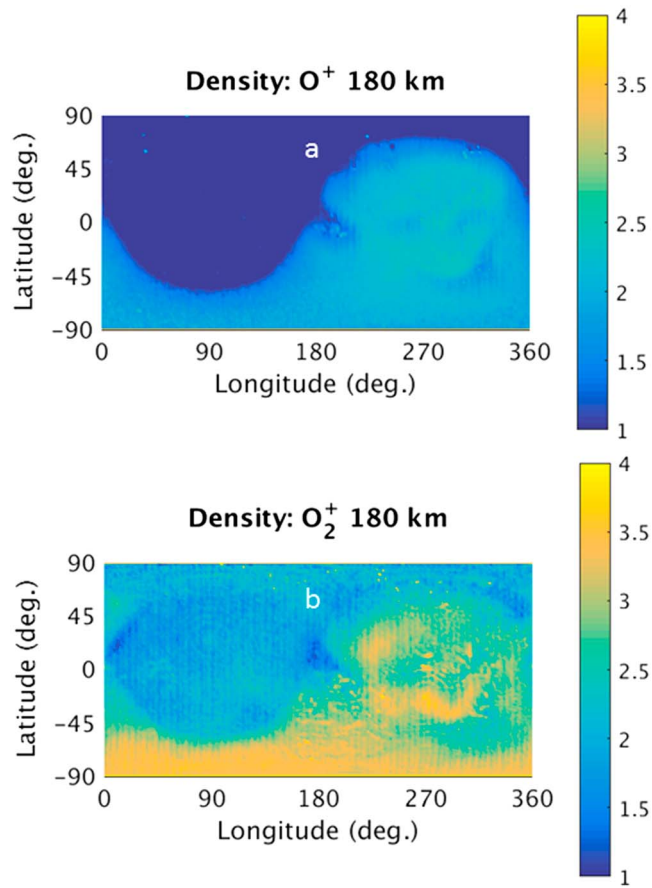


**Figure 8.** (a)  $O^+$  and (b)  $O_2^+$  density ( $\#/cm^3$ ) contours at an altitude of 180 km shown in  $\log_{10}$  levels. The contours are the result of using the nominal MTGCM/S&C profile.

dashed lines display the  $O_2^+$  distribution functions. There is no obvious acceleration relative to each simulation or even each species. The red lines from the MTGCM/S&C profile labeled MTGCM consistently shows a higher value throughout most of the energy range. This is in agreement with the loss rates shown in Table 1.

There are some interesting features displayed by the distribution functions. The bump found in the distribution function between 1 and 10 keV is from the energetic ions removed from the planet in the direction of the convection electric field. This feature is often referred to as the plume. In this region the  $O_2^+$  flux is the same for both simulations. However, the  $O^+$  still displays the ratio of the loss rates listed in Table 1. In the energy

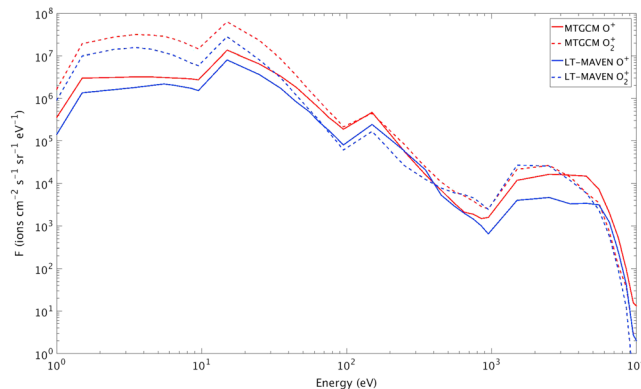


**Figure 9.** Escaping ion flux ( $\#/cm^2 s sr eV$ ) distribution for  $O_2^+$  (dashed lines) and  $O^+$  (solid lines) plotted for the nominal  $T_e$  profile (red) and the low  $T_e$  fit to MAVEN data (blue) as a function of energy.

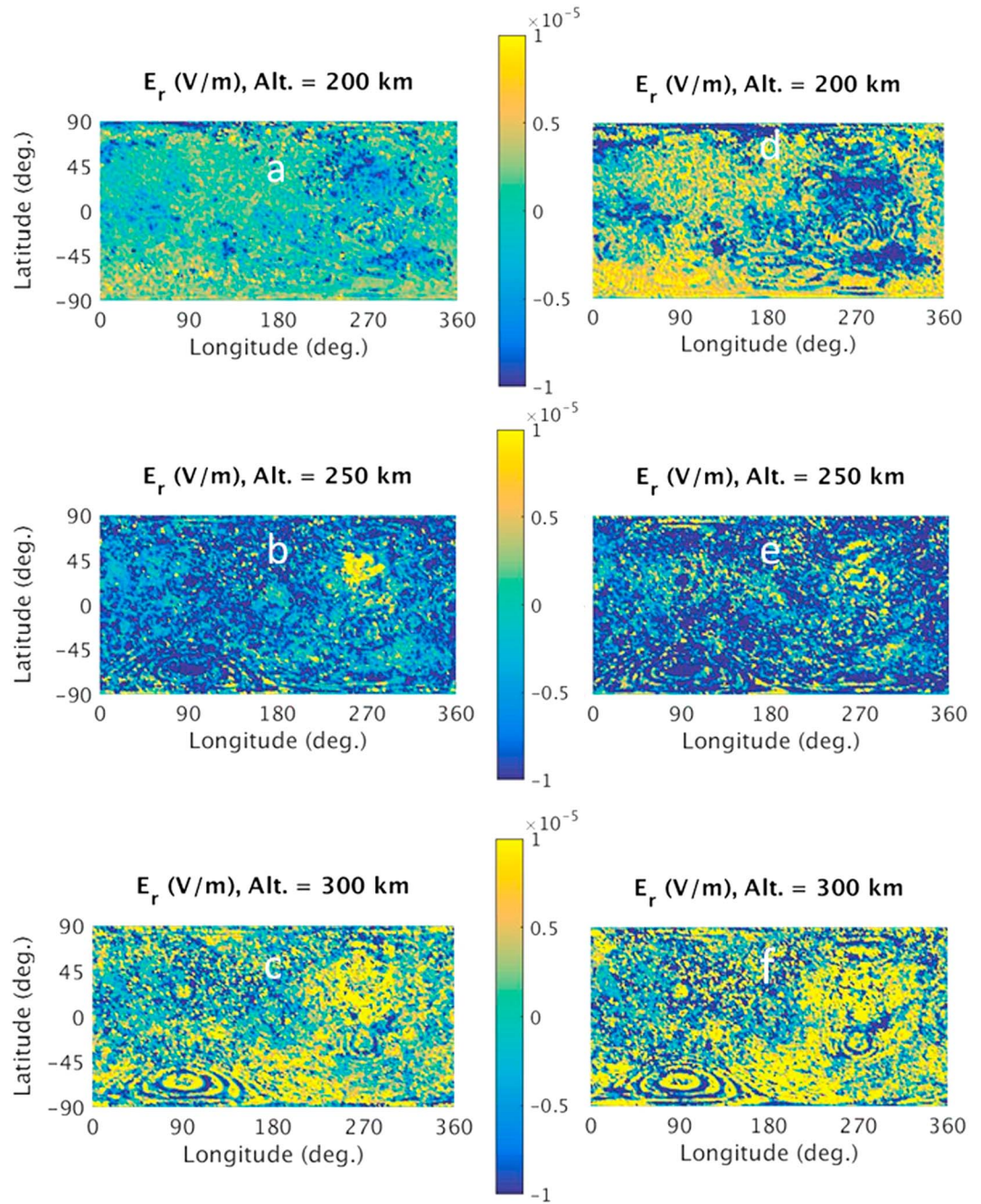


**Figure 10.** Contour plots of  $\nabla p_e$  driven ambipolar radial electric field at three altitudes (200 km, 250 km, and 300 km). (a–c) From the simulation using the low  $T_e$  MAVEN temperature fit. (d–f) From the simulation using the nominal MTGCM/S&C fit.

region from 60 eV to 600 eV, one notes that the loss fluxes for the two ion species become comparable for both simulation situation. This is unexpected.

To summarize, changing the electron temperature profile from a rather warm profile, MTGCM/S&C, to one representing the lower limits of the electron temperatures measured by MAVEN and reported in *Ergun et al.* [2015, 2016] results in changes in the ion loss rate from Mars by a factor of roughly 2. Further, the composition ratio (the ratio of  $O^+$  to  $O_2^+$ ) changes from 1:3 to 1:2. However, there has not been much evidence to indicate why these changes take place. Figure 3 offers a suggestion as one sees the electric field driven by the  $\nabla p_e$  term change sign and magnitude as a function of altitude with the nominal profile producing the most pronounced swings in the electric field. Still the profiles shown in Figure 3 are at the subsolar

point which provides limited insight. To address the issue of the ambipolar electric fields, planes of  $E_r$  produced by the  $\nabla p_e$  term are plotted at three altitudes (200 km, 250 km, and 300 km), Figure 10. Figures 10a–10c are from the simulation using the low  $T_e$  MAVEN temperature fit. Figures 10d–10f are from the simulation using the nominal MTGCM/S&C fit.

Figures 10a and 10d offer some insight into why the two electron temperature profiles produce differing ion loss rates. In Figure 10a one sees a few localized places where there is a positive radial electric field. There are also localized places where there is a negative radial electric field. However, much of the surface has  $E_r$  at or very near zero. Examining Figure 10d, one finds a very different situation. There are places with strong negative  $E_r$ , but larger regions where the  $E_r$  is positive and strong. It has been found in past simulation work by both *Brecht and Ledvina* [2006, 2012] and *Liu et al.* [2001] as well as from data [*Lundin et al.*, 2004] that the altitude where the ion removal is strongest is between 200 and 250 km.

At 250 km Figures 10b and 10e show similar results with the bulk of the plane displaying negative radial electric fields with a value of  $-10 \mu\text{V/m}$ . This is consistent with Figure 3. One does see some regions where there is a positive radial electric field reaching  $10 \mu\text{V/m}$ . The 300 km plots in Figures 10c and 10f display a preponderance of positive radial electric fields again with peak value of  $10 \mu\text{V/m}$ . The structure seen in Figures 10c and 10f mimics that of the structure revealed in Figure 7b. Close inspection of Figures 10c and 10f reveals that for the nominal electron temperature case, Figure 10f, one sees that the dayside ( $180^\circ$ – $60^\circ$  longitude) has a larger region of positive  $E_r$  values. There seems to be no difference on the nightside.

Figures 10a and 10d (200 km) show a neutral to strongly positive net field below a net negative  $E_r$  at 250 km (Figures 10b and 10e) and then a strong positive field at 300 km (Figures 10c and 10f) for both simulations. This is consistent with Figure 3. All of this suggests that to remove more ions, one needs to get them moving upward at lower altitudes where the density is higher. It appears this injects the ions into a region above 275 km where the radial electric field can really begin to accelerate them. At 300 km the positive  $E_r$  from the  $\nabla p_e$  covers a larger area in the nominal case than in the low  $T_e$  MAVEN case. This may explain the changing loss rates with respect to the electron temperature profile. In Figures 10c and 10f it is not obvious whether the maximum fields are the same, as the color bar hides small difference. However, Figure 3 would suggest that the fields are stronger in the nominal case by a factor of  $\sim 2$ . This does not seem to be the case when plasma advection is included; again see Figures 10c and 10f. Figure 9 suggests that there is not a difference in acceleration but simply a difference in the number of ions being removed from the ionosphere. The fact that Figures 10c and 10f do not indicate significant differences in the field strength but differences in the area covered suggests that the nominal case simply leads to more ions coming from a broader region of the Martian ionosphere.

## 6. Discussion and Conclusions

The role of the electron temperature have been investigated by changing the  $T_e$  profile used in the hybrid particle code HALFSHEL. The new MAVEN electron temperature data coupled with the fit function from *Ergun et al.* [2015] provided an opportunity to assess the sensitivity of the solar wind interaction with Mars to changes in the electron temperature.

Interesting changes occurred in the simulations when the ionospheric electron temperature profile was modified. Some of the results were unexpected and some were expected. The expected changes were that the temperature dependence of several of the recombination reactions did make a difference in the densities of the oxygen ion balance found in the ionosphere, Figure 2. This had been predicted by a variety of authors over the years and certainly by *Ergun et al.* [2016]. *Ergun et al.* [2016] had also suggested that ratio of oxygen ions lost to space would change. The HALFSHEL results confirmed this. With the low  $T_e$  profile motivated by the MAVEN data, it was found that the ratio of  $\text{O}_2^+$  to  $\text{O}^+$  lost changed to 2:1 rather than the 3:1 ratio reported earlier by *Brecht et al.* [2016]. However, the low  $T_e$  MAVEN fit also had enough noise to argue that in many places, ratio of oxygen ion species could approach 1:1. The oxygen ion loss rate was reduced by a factor of 2 when the profile was changed from that determined by using the MTGCM/S&C temperature profile to the fit, equation (2), of the low  $T_e$  MAVEN data, Table 1.

It is found, as expected, that the photochemistry changes with differing  $T_e$  profiles, Figure 2. The chemical changes were found only in specific altitude ranges between  $\sim 250$  km and 180 km. Advection of the

plasma modifies the typical photochemical altitude profile, Figure 2. Instead of finding  $O_2^+$  dropping to densities of 1 by 350 km altitude, Figure 2, one sees advection of high densities to altitudes of 500 km or more, Figure 6. This result is in agreement with data [Benna *et al.*, 2015; Ergun *et al.*, 2016].

An unexpected result was that examination of the plasma spatial distribution and altitude dependence did not offer any insight into the changes of oxygen ion composition ratio or the total loss rate driven by the changing  $T_e$  profile. Examination of the ambipolar radial electric field,  $E_r$ , created by the  $\nabla p_e$  term does indicate a possible explanation. Figure 10 illustrated that changing the electron temperature profile did modify the strength of  $E_r$  in the altitude range of 200 km to 250 km. This is precisely the range where a majority of the escaping ions are launched. In addition, the ambipolar  $E_r$  is found to be positive over a larger region of the dayside of the planet for the MTGCM/S&C profile.

Only the radial electric field created by the  $\nabla p_e$  was examined. The other components of this ambipolar source of electric field can and probably do play a role in the structure and escape of the ions as they interact both with the electric fields and the magnetic fields intrinsic of the Martian system (crustal magnetic fields) and those imposed by the solar wind.

Finally, it was noted that as one progressed from simulations with no ambipolar electric field,  $\nabla p_e = 0$ , to the high temperature profiles often used in the past [cf. Brecht *et al.*, 2016], the noise in the loss rates of each oxygen ion species was reduced. The reason for this result is not clear. One numerical test was performed. The test required the  $T_e$  profile to remain the same, MTGCM/S&C, but the temperature used in recombination chemistry, equation (3)–(5), was set to very cold. In this experiment it was found that the total loss rate did not change from our nominal loss rate but the ratio between  $O_2^+$  and  $O^+$  went to nearly one (1). The ion density profiles were very strongly modified in the test case thus changing the  $\nabla p_e$ -driven electric fields.

It is clear that future research should address the changes that occur as one tests the MAVEN motivated  $T_e$  profile for varying crustal magnetic field orientations. The use of differing neutral atmosphere models representing changes in the EUV flux is also important because the chemistry is dependent on both the neutral densities and the ionization cross sections as well as the  $T_e$  profiles. It would be very interesting to change the transition altitude where the electron temperature equation, equation (1), ceases to be used from the current 500 km to 250 km. In order to do so the temperature equation would need to be augmented to include thermal conduction physics and cooling due to collisions; see Matta *et al.* [2014] for a detailed discussion of these terms.

As more information becomes available about the nightside temperatures, the assumption of a constant electron temperature profile around the planet could be relaxed. A more realistic nightside  $T_e$  profile may lead to better agreement between the HALFSHEL simulations [see Ledvina *et al.*, 2017] and the data reported by Brain *et al.* [2015]. At present, the HALFSHEL results show a larger ion loss on the nightside than does Brain *et al.* [2015]. Finally, it would be very interesting to simulate Mars with even finer resolution than we have used in the past. While we have seen in the past that the loss rates did not change with improved resolution, it would be still interesting to investigate changes in the plasma and magnetic structure when the Cartesian grid is changed to 50 km and the spherical grid had an angular resolution of less than  $1^\circ$ .

In conclusion, the  $T_e$  profile is an important parameter for understanding the dynamics within the Martian ionosphere. The chemistry did change as predicted and the advection of plasma was modified leading to changes in the total loss rate by a factor of 2. The change in the  $T_e$  profile affected the ratio of  $O_2^+/O^+$ . The ratio was 3:1 with the nominal electron temperature profile and became 2:1 with the MAVEN motivated profile. This change brought the simulation results in line with data [cf. Benna *et al.*, 2015; Nilsson *et al.*, 2011]. Finally, it was shown that the ambipolar electric field as represented by the  $\nabla p_e$  term in the electric field equation, equation (6), does play a significant role in the ion loss from Mars. These results indicate, once again, that the Martian system is a sensitive system and predicting what the combination of active chemistry and plasma advection driven by the solar wind might do is complex undertaking.

## References

- Acuña, M., et al. (1998), Magnetic field and plasma observations at Mars: Initial results of the Mars Global Surveyor mission, *Science*, 279, 1676.
- Acuña, M. H., et al. (1999), Global distribution of crustal magnetization discovered by the Mars Global Surveyor MAG/ER experiment, *Science*, 284(5415), 790–793, doi:10.1126/science.284.5415.790.

## Acknowledgments

The authors acknowledge the important contribution made by Stephen Bougher of the University of Michigan in providing the neutral atmosphere used in this research. S.H. Brecht and S.A. Ledvina would like to acknowledge the support from NASA contract NNH12CF43C. S.A.L. acknowledges the support from the MAVEN mission. The authors would like to acknowledge the computational support provided by the NASA Advanced Supercomputer facility, NAS, at NASA Ames Research Center Moffett field CA. Finally, data from which the results of this paper are taken are available upon contact with S.H.B. or S.A.L.

- Benna, M., P. R. Mahaffy, J. M. Grebowsky, J. L. Fox, R. V. Yelle, and B. M. Jakosky (2015), First measurements of composition and dynamics of the Martian ionosphere by MAVEN's neutral gas and ion mass spectrometer, *Geophys. Res. Lett.*, *42*, 8958–8965, doi:10.1002/2015GL066146.
- Bertaux, J.-L., F. Leblanc, O. Witasse, E. Quemerais, J. Liliensten, S. A. Stern, B. Sandel, and O. Korablev (2005), Discovery of an aurora on Mars, *Nat. Lett.*, *435*, 790, doi:10.1038/nature03603.
- Bell, J. M., S. W. Bougher, and J. R. Murphy (2007), Vertical dust mixing and the interannual variations in the Mars thermosphere, *J. Geophys. Res.*, *112*, E12002, doi:10.1029/2006JE002856.
- Bougher, S. W., G. Keating, R. Zurek, J. Murphy, R. Haberle, J. Hollingsworth, and R. T. Clancy (1999a), Mars Global Surveyor aerobraking: Atmospheric trends and model interpretation, *Adv. Space Res.*, *23*, 1887–1897, doi:10.1016/S0273-1177(99)00272-0.
- Bougher, S. W., S. Engel, R. G. Roble, and B. Foster (1999b), Comparative terrestrial planet thermospheres: 2. Solar cycle variation of global structure and winds at equinox, *J. Geophys. Res.*, *104*, 16,591–16,611, doi:10.1029/1998JE001019.
- Bougher, S. W., S. Engel, R. G. Roble, and B. Foster (2000), Comparative terrestrial planet thermospheres: 3. Solar cycle variation of global structure and winds at solstices, *J. Geophys. Res.*, *105*, 17,669–17,692, doi:10.1029/1999JE001232.
- Bougher, S. W., R. G. Roble, and T. J. Fuller-Rowell (2002), Simulations of the upper atmospheres of the terrestrial planets, in *Atmospheres in the Solar System, Comparative Aeronomy, Geophys. Monogr. Ser.*, vol. 130, edited by M. Mendillo, A. F. Nagy, and J. H. Waite Jr., pp. 261–288, AGU, Washington, D. C.
- Bougher, S. W., S. Engel, D. P. Hinson, and J. R. Murphy (2004), MGS radio science electron density profiles: Interannual variability and implications for the Martian neutral atmosphere, *J. Geophys. Res.*, *109*, E03010, doi:10.1029/2003JE002154.
- Bougher, S. W., J. M. Bell, J. R. Murphy, M. A. Lopez-Valverde, and P. G. Withers (2006), Polar warming in the Mars thermosphere: Seasonal variations owing to changing isolation and dust distributions, *Geophys. Res. Lett.*, *33*, L02203, doi:10.1029/2005GL024059.
- Bougher, S. W., et al. (2008), Neutral upper atmosphere and ionosphere modeling, *Space Sci. Rev.*, *139*, 107–141, doi:10.1007/s11214-008-9401-9.
- Brain, D. A., J. S. Halekas, L. M. Petcolas, R. P. Lin, J. G. Luhmann, D. L. Mitchell, G. T. Delory, S. W. Bougher, M. H. Acuña, and H. Rème (2006), On the origin of aurorae on Mars, *Geophys. Res. Lett.*, *33*, L01201, doi:10.1029/2005GL024782.
- Brain, D. A., et al. (2015), The spatial distribution of planetary ion fluxes near Mars observed by MAVEN, *Geophys. Res. Lett.*, *42*, 9142–9148, doi:10.1002/2015GL065293.
- Brecht, S. H., and S. A. Ledvina (2006), The solar wind interaction with the Martian ionosphere/atmosphere, *Space Sci. Rev.*, *126*, 15.
- Brecht, S. H., and S. A. Ledvina (2010), The loss of water from Mars: Numerical results and challenges, *Icarus*, *206*(1), 164–173, doi:10.1016/j.icarus.2009.04.028.
- Brecht, S. H., and S. A. Ledvina (2012), Control of ion loss rates from Mars during solar minimum, *Earth Planets Space*, *64*, 165–178.
- Brecht, S. H., and S. A. Ledvina (2014), The role of the Martian crustal magnetic fields in controlling ionospheric loss, *Geophys. Res. Lett.*, *41*, 5340–5346, doi:10.1002/2014GL060841.
- Brecht, S. H., S. A. Ledvina, and S. W. Bougher (2016), Ionospheric loss from Mars as predicted by hybrid particle simulations, *J. Geophys. Res. Space Physics*, *121*, 10,190–10,208, doi:10.1002/2016JA022548.
- Carlsson, E., et al. (2006), Mass composition of the escaping plasma at Mars, *Icarus*, *182*, 320–328.
- Cravens, T. E., J. U. Kozyra, A. Nagy, T. Gombosi, and M. Kurtz (1987), Electron impact ionization in the vicinity of comets, *J. Geophys. Res.*, *92*, 7341–7353, doi:10.1029/JA092iA07p07341.
- Dong, C., S. W. Bougher, Y.-J. Ma, G. Toth, A. F. Nagy, and D. Najib (2014), Solar wind interaction with Mars upper atmosphere: Results from the one-way coupling between the multi-fluid MHD model and the MTGCM model, *Geophys. Res. Lett.*, *41*, 2708–2715, doi:10.1002/2014GL059515.
- Ergun, R. E., M. W. Morooka, L. A. Andersson, C. M. Fowler, G. T. Delory, D. J. Andrews, A. I. Eriksson, T. McEnulty, and B. M. Jakosky (2015), Dayside electron temperature and density profiles at Mars: First results from the MAVEN Langmuir probe and waves instrument, *Geophys. Res. Lett.*, *42*, 8846–8853, doi:10.1002/2015GL065280.
- Ergun, R. E., M. W. Morooka, L. A. Andersson, C. M. Fowler, G. T. Delory, D. J. Andrews, A. I. Eriksson, T. McEnulty, and B. M. Jakosky (2016), Enhanced  $O_2^+$  loss at Mars due to ambipolar electric field from electron heating, *J. Geophys. Res. Space Physics*, *121*, 4668–4678, doi:10.1002/2016JA022349.
- Fowler, C. M., et al. (2015), The first in situ electron temperature and density measurements of the Martian nightside ionosphere, *Geophys. Res. Lett.*, *42*, 8854–8861, doi:10.1002/2015GL065267.
- Fox, J. L. (1993), The production and escape of nitrogen atoms on Mars, *J. Geophys. Res.*, *98*, 3297–3310, doi:10.1029/92JE02289.
- Halekas, J. S., D. A. Brain, R. P. Lin, J. G. Luhmann, and D. L. Mitchell (2008), Distribution and variability of accelerated electrons at Mars, *Adv. Space Res.*, *41*, 1347.
- Jakosky, B. M., J. M. Grebowsky, J. G. Luhmann, and D. A. Brain (2015), Initial results from the MAVEN mission to Mars, *Geophys. Res. Lett.*, *42*, 8791–8802, doi:10.1002/2015GL065271.
- Leblanc, F., O. Witasse, J. Winningham, D. Brain, J. Liliensten, P.-L. Blély, R. A. Frahm, J. S. Haledas, and J. L. Bertaux (2006), Origins of the Martian aurora observed by the spectroscopy for investigation of characteristics of the atmosphere of Mars (SPICAM) on board Mars Express, *J. Geophys. Res.*, *111*, A09313, doi:10.1029/2006JA001763.
- Leblanc, F., et al. (2008), Observations of aurorae by SPICAM ultraviolet spectrograph on board Mars Express: Simultaneous ASPERA-3 and MARSIS measurements, *J. Geophys. Res.*, *113*, A08311, doi:10.1029/2008JA013033.
- Ledvina, S. A., S. H. Brecht, D. A. Brain, and B. M. Jakosky (2017), Ion escape rates from Mars: Results from hybrid simulations compared to MAVEN observations, *J. Geophys. Res. Space Physics*, *122*, doi:10.1002/2016JA023521.
- Liu, Y., A. F. Nagy, T. I. Gombosi, D. L. DeZeeuw, and K. G. Powell (2001), The solar wind interaction with Mars: Results of the three-dimensional three species MHD studies, *Adv. Space Res.*, *27*, 2689–2692.
- Lundin, R., et al. (2004), Solar wind-induced atmospheric erosion at Mars: First results from ASPERA-3 on Mars express, *Science*, *305*, 1933–1936, doi:10.1126/science.1101860.
- Lundin, R., et al. (2006a), Plasma acceleration above Martian magnetic anomalies, *Science*, *311*, 980–983, doi:10.1126/science.1122071.
- Lundin, R., et al. (2006b), Auroral plasma acceleration above Martian magnetic anomalies, *Space Sci. Rev.*, *126*, 333, doi:10.1007/s11214-006-9086-x.
- Ma, Y., A. F. Nagy, K. C. Hansen, and D. L. DeZeeuw (2002), Three-dimensional multispecies MHD studies of the solar wind interaction with Mars in the presence of crustal fields, *J. Geophys. Res.*, *107*(A10), 1282, doi:10.1029/2002JA009293.
- Ma, Y., A. F. Nagy, I. V. Sokolov, and K. C. Hansen (2004), Three-dimensional, multispecies, high spatial resolution MHD studies of the solar wind interaction with Mars, *J. Geophys. Res.*, *109*, A07211, doi:10.1029/2003JA010367.
- Matta, M., M. Galand, L. Moore, M. Mendillo, and P. Withers (2014), Numerical simulations of ion and electron temperatures of Mars: Multiple ions and diurnal variations, *Icarus*, *227*, 78–88, doi:10.1016/j.icarus.2013.09.006.

- Mitchner, M., and C. H. Kruger Jr. (1973), *Partially Ionized Gases*, pp. 173–182, John Wiley, New York.
- Nilsson, H., N. J. T. Edberg, G. Stenberg, S. Barabash, M. Holmström, Y. Futaana, R. Lundin, and A. Fedorov (2011), Heavy ion escape from Mars, influence from solar wind conditions and crustal magnetic fields, *Icarus*, *215*, 475–484, doi:10.1016/j.icarus.2011.08.003.
- Otsuka, Y., S. Kawamura, N. Balan, S. Fukao, and G. J. Baily (1998), Plasma temperature variations in the ionosphere over the middle and upper atmosphere radar, *J. Geophys. Res.*, *103*, 20,705–20,713, doi:10.1029/98JA01748.
- Purucker, M., D. Ravat, H. Frey, C. Voorhies, T. Sabaka, and M. Acuña (2000), An altitude-normalized magnetic map of Mars and its interpretation, *Geophys. Res. Lett.*, *27*, 2449, doi:10.1029/2000GL000072.
- Shinagawa, H., and T. E. Cravens (1989), A one-dimensional multi-species magnetohydrodynamic model of the dayside ionosphere of Mars, *J. Geophys. Res.*, *94*, 6506, doi:10.1029/JA094iA06p06506.
- Shunk, R. W., and A. F. Nagy (2000), *Ionospheres*, 1st ed., pp. 89–92, Cambridge Univ. Press, Cambridge, U. K.
- Singhal, R. P., and R. C. Whitten (1988), Thermal structure of the ionosphere of Mars: Simulations with one- and two-dimensional models, *Icarus*, *74*, 357–364.
- Spitzer, L. (1962), *Physics of Fully Ionized Gases*, 2nd ed., 127 pp., Interscience Publ., New York.
- Strangeway, R. (1996), Collisional joule dissipation in the ionosphere of Venus: The importance of electron heat conduction, *J. Geophys. Res.*, *101*, 2279, doi:10.1029/95JA02587.